Chemistry Europe
European Chemical Societies Publishing
Batteries & Supercaps

RESEARCH ARTICLE OPEN ACCESS

Demonstrating the Performance of Aspartic-Acid Functionalized Naphthalene Diimide in a Near-Neutral Flow Battery

Mahsa Shahsavan[1] | Cedrik Wiberg[2] | Andrea Hamza[3] | Aapo Poskela[1] | Johan Hjelm[4] | Pekka Peljo[1,5]

[1]Department of Mechanical and Materials Engineering, Faculty of Technology, University of Turku, Finland | [2]Rivus Batteries, Gothenburg, Sweden | [3]Institute of Organic Chemistry, HUN-REN Research Centre for Natural Sciences, Budapest, Hungary | [4]Department of Energy Conversion and Storage, Technical University of Denmark, Lyngby, Denmark | [5]Department of Chemistry and Materials Science, Aalto University, Espoo, Finland

Correspondence: Andrea Hamza (hamza.andrea@ttk.hu) | Pekka Peljo (pekka.peljo@utu.fi; pekka.peljo@aalto.fi)

Received: 30 September 2025 | **Revised:** 15 December 2025 | **Accepted:** 25 December 2025

Keywords: aqueous organic flow battery | aspartic acid functionalization | high-solubility negolyte | naphthalene diimide (NDI)

ABSTRACT

The performance of the negatively charged aspartic acid-functionalized naphthalene diimide (ASP-NDI) in a flow battery is investigated in this article. The high concentration ASP-NDI/ferrocyanide flow battery presented cycled for 79.8 days with an average coulombic efficiency of 99.9% and an energy efficiency of 87.5% at 20 mA cm^{-2} while accessing an over 90% of the theoretical capacity of ASP-NDI with a capacity fade rate of 0.0275% per day that is the lowest reported for the NDI-based flow batteries to date.

1 | Introduction

Renewable energy sources such as solar and wind hold great promise in transitioning to a more sustainable future. However, the fact that these energy sources are not always available makes them unreliable sources of energy. Therefore, improving energy storage technology can greatly impact how well renewable energy sources can be integrated into the grid [1, 2]. For the past couple of years, flow batteries have emerged as a promising solution to address the intermittent nature of renewable energy sources. Their unique advantage of decoupling energy and power makes them highly suitable for large-scale applications [3–5]. Commercial flow batteries rely on vanadium-based redox couples for both the positive and the negative side, known as posolyte and negolyte, respectively [6]. However, the pursuit of more cost-effective and versatile alternatives has led researchers to explore organic redox-active molecules. Organic molecules are attractive since their chemical and electrochemical properties can be tailored through different functional groups, enabling researchers to modify their properties to align with the requirements of the flow battery [7]. This tunability is particularly important in flow batteries where charge storage density is determined by the solubility of the redox couple as well as the number of electrons exchanged in the redox reactions. Therefore, reasonably soluble molecules capable of reversibly exchanging two or more electrons in redox reactions are attractive research targets to achieve improved energy storage density. Anthraquinones, phenazines, and viologens have already emerged as notable candidates, exhibiting satisfactory performance as two-electron storage materials [8–13]. Recently, researchers introduced a new class of organic negolytes designed to reversibly store two electrons. Drawing inspiration from n-type organic semiconducting materials, water-soluble naphthalene diimides (NDIs) can be a good choice for flow batteries [14–21]. NDI's extended π-conjugation over polycyclic aromatic rings on one hand, is anticipated to provide structural stability during the reduction process and on the other hand, can result in the self-association of the aromatic cores. The electrochemical characteristics of NDIs can be adjusted through core substitutions, while selecting an appropriate side chain on the imide nitrogen can influence solubility and potentially prevent self-association [14]. The previously studied NDIs were either positively charged and/or suffered from low solubility [15, 17]. The recent demonstration of the negatively charged NDI

from our group, the NDI functionalized with gamma-aminobutyric acid (GABA-NDI), exhibited increased solubility; however, its solubility has not reached the level required for industrial applications [16]. To enhance the water solubility of NDIs, in this work, we incorporated aspartic acid into the redox-active core of NDI. Functionalization of NDI with aspartic acid (ASP-NDI) led to a nearly twofold increase in solubility in water compared to its GABA analog, along with improved chemical stability and reduced self-association, due to the additional carboxylate group that increases its hydrophilicity. Flow battery measurements using ASP-NDI and sodium ferrocyanide ($Na_4[Fe(CN)_6]$) demonstrated high capacity utilization (>95% of theoretical capacity) over extended cycling, with average coulombic efficiencies exceeding 99% and energy efficiencies in the range of 86%–91% for cycling at 20 mA/cm^2. These results highlight ASP-NDI as a promising, high-performance, two-electron negolyte for aqueous organic flow batteries, with potential for long-term stable operation when paired with a suitable membrane.

2 | Results and Discussion

2.1 | Synthesis of ASP-NDI

Functionalization of NDI with aspartic acid occurred in a one-step synthesis (Scheme 1). For the synthesis, potassium hydroxide (KOH) (5.10 g, 82 mmol) was added to a suspension of aspartic acid (10.91 g, 82 mmol) in water (40 mL) and stirred at room temperature until all aspartic acid dissolved (around 10–15 min). A suspension of 1,4,5,8-naphthalenetetracarboxylic acid dianhydride (10.72 g, 40 mmol), in 400 mL DMSO (10 mL DMSO for 1 mmol of 1,4,5,8-naphthalenetetracarboxylic acid dianhydride) was heated to 70°C until all of it dissolved. After that the aqueous solution of the dissolved aspartic acid was added dropwise to the DMSO solution. Within 5 min some crystals were formed. Then the reaction mixture was heated at 120°C, for 1 h until the formed crystals had dissolved, and then the temperature was raised to 140°C and left to stir at this temperature for 24 h. Reaction mixture was cooled to room temperature, product was filtered and washed with DMSO (1 × 40 mL), isopropanol (2 × 40 mL) then diethyl ether (2 × 40 mL) (washing with ether was performed to boost drying) and dried. Yielding 13 g (50%) of product as dipotassium salt. The product as dipotassium salt (13 g) was acidified to pH 1.4 with 3 M HCl (around 30 mL) and left to stand for 1 h. The product was filtered. Crystals were taken from the filter to the flask and stirred with water, then left to stand for 2 h. Product was filtered and dried in air (yield 9,6 g (48%)). The structure of the synthesized molecule was confirmed with ^{1}H-NMR and LC/MS (Figures S1–S3).

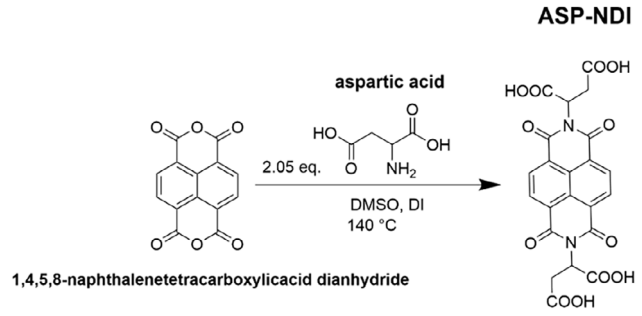

SCHEME 1 | Synthesis of ASP-NDI.

2.2 | Measuring the solubility of ASP-NDI.

For measuring the solubility of ASP-NDI in DI water, ^{1}H-NMR was done with 2,3,5,6-tetramethylpyrazine (TMPz) as an internal reference, and the solubility of 1.07 M for ASP-NDI could be obtained in DI water (Figure S4). The solubility of ASP-NDI in 1 M ammonium chloride (NH_4Cl) was not measured with NMR, but a maximum concentration of 700 mM in 1 M NH_4Cl as a supporting electrolyte could be prepared by the addition of solid to the electrolyte. The solubility of ASP-NDI is 1.8 and 2.8 times higher than the solubility of GABA-NDI under the same conditions, respectively. To deprotonate ASP-NDI, by adding ammonia (NH_3) to the solution, the pH of the electrolyte was adjusted to 7. The enhanced solubility of ASP-NDI is due to the presence of one more carboxylic acid group in comparison to GABA-NDI, which makes the aspartic acid (ASP) more hydrophilic than γ-aminobutyric acid (GABA) [22, 23]. In addition, NH_4Cl was selected as the supporting electrolyte because ammonium cations (NH_4^+) are known to suppress the formation of large electrochemically inactive aggregates in the other study done on NDIs [15]. Prior studies have also shown that NH_4^+ increases the solubility of redox-active anions such as AQDS and ferrocyanide compared with alkali-metal cations. This effect has been attributed to differences in the inner hydration-shell structure of NH_4 [24, 25]. In contrast, K^+ has been reported to promote aggregation and potassium trapping in glycine–NDI systems [17]. The use of NH_4^+ therefore, mitigates aggregation of reduced NDI species and supports higher solubility.

2.3 | Electrochemical characterization.

Cyclic voltammograms (CV) of ASP-NDI at pH 7 in 1 M NH_4Cl show two reversible redox reactions, which remain almost unaffected by the increase in scan rate, indicating fast electron-transfer kinetics (Figure 1a). The redox potentials of the molecule at the concentration of 5 mM are located at −493 and −609 mV versus Ag/AgCl (Sat. KCl with a potential of 197 mV vs. SHE) (−296 and −412 mV vs. SHE). Although the peaks remain almost unchanged in the scan rate-normalized CVs (Figure 1b), the concentration-normalized CVs (Figure S5) exhibit a decrease in peak current with increasing concentration. Combined with the diffusion coefficients evaluated from the Randles–Ševčík equation (Table S1), this behavior indicates a self-association tendency of the NDI molecules at higher concentrations [16]. Moreover, as previously shown, the increase in the concentration results in an increase in the peak separation with the first reduction potential moving to more positive potentials and the second to more negative potentials (Figure S6) [15].

Rotating disk electrode (RDE) measurements were conducted to gain further insights into the electrochemical properties of the synthesized molecule. As indicated by the voltammograms in Figure 2, increasing the concentration causes the first and second reductions to merge, particularly at higher scan rates. Utilizing the Levich equation (Figure S7), an average diffusion coefficient of 3.61×10^{-6} cm^2 s^{-1} is derived for the oxidized ASP-NDI at a concentration of 1 mM, which is similar to the average diffusion coefficient of the oxidized GABA-NDI at the same concentration [16]. However, ASP-NDI at the concentration of 5 mM yields a diffusion coefficient of 2.31×10^{-6} cm^2 s^{-1}. The lower diffusion coefficient obtained for the 5 mM voltammogram further supports the self-association of the molecule at higher concentrations.

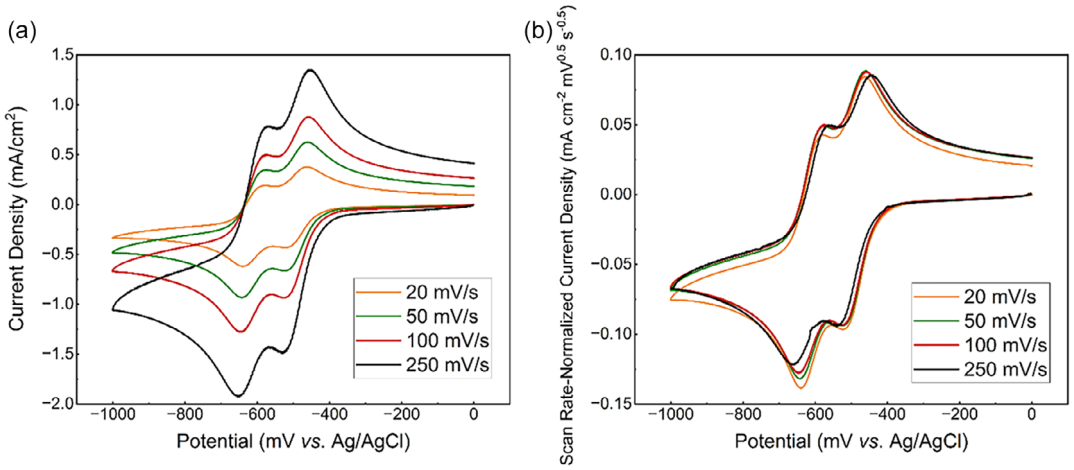

FIGURE 1 | (a) CV of 5 mM ASP-NDI in 1 M NH_4Cl at different scan rates. (b) Scan rate-normalized CVs of 5 mM ASP-NDI in 1 M NH_4Cl.

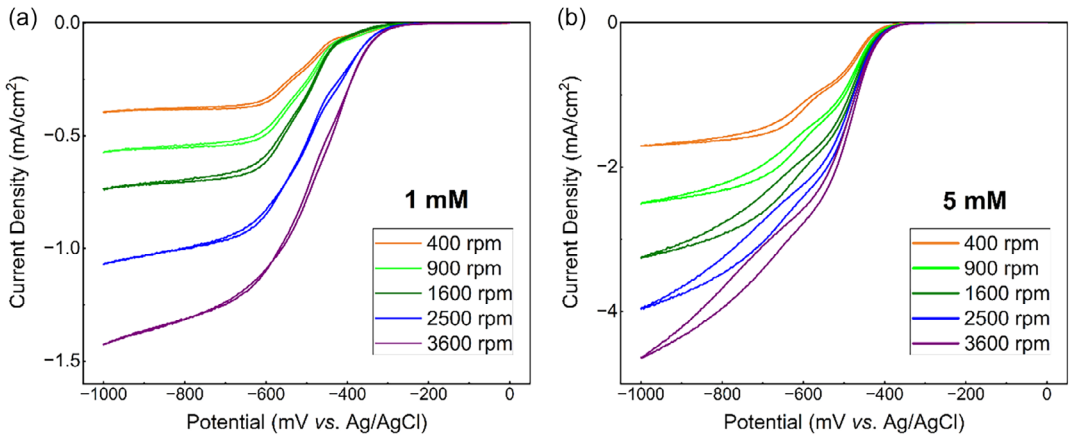

FIGURE 2 | RDE measurements in 1 M NH_4Cl at different rotation rates at the scan rate of 5 mV/s. (a) 1 mM and (b) 5 mM of ASP-NDI.

2.4 | pH studies on ASP-NDI.

The variation of redox potentials with pH is depicted in Figure 3, indicating consistent redox activity of the molecule up to pH 10.5. The Pourbaix diagram of ASP-NDI (Figure S8) shows that the potential drop for the first reduction between pHs 7–8.5 and 8.5–10.5 is –0.9 and –12 mV/pH, respectively; and for the second reduction between pHs 7–10.5 is –1.1 mV/pH which shows that the electrochemical reduction and oxidation of ASP-NDI is not sensitive to the change in pH at this range, similarly to NDI with quaternary amine sidechains [14]. However, the ^{1}H-NMR analysis of ASP-NDI at pH 10.5 (Figure S9) reveals the appearance of new peaks after 24 h. These new peaks arise from the hydrolysis of the NDI imide rings in alkaline pH, resulting in ring-opened carboxylate/amide species that indicate molecular degradation; while this hydrolysis can be reversible upon returning to neutral pH, prolonged exposure to high pH promotes further irreversible degradation that leads to permanent loss of redox activity [26–29]. Therefore, both CV and ^{1}H-NMR confirm that prolonged exposure to pH 10.5 can significantly diminish its redox activity, and battery operation is therefore limited to pHs below 10.

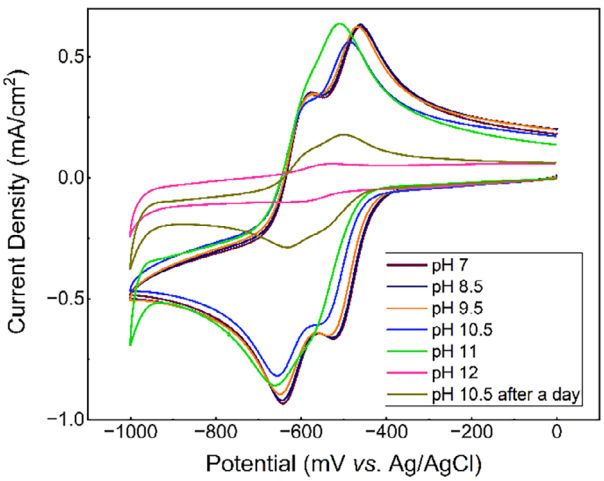

FIGURE 3 | pH dependency of 5 mM ASP-NDI in 1 M NH_4Cl and 0.5 M ammonium phosphate buffer at 50 mV/s.

2.5 | Comparison between ASP-NDI and GABA-NDI

A comparison between the CVs of GABA-NDI and ASP-NDI is made in Figure 4. The average redox potential for GABA-NDI is –485.5 mV, while it is –551 mV for ASP-NDI, leading to slightly increased total cell voltage. Moreover, NMR spectra obtained at various concentrations of ASP-NDI and GABA-NDI are shown in Figure S10. According to the previous studies, less self-association is seen in ASP-NDI due to the decreased broadening and the shift of

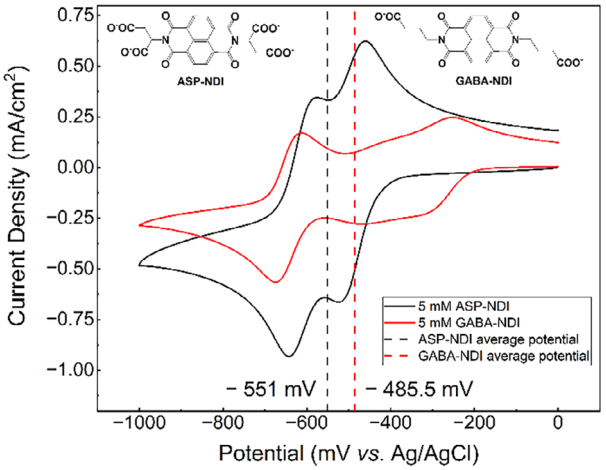

FIGURE 4 | CV of ASP-NDI and GABA-NDI at 50 mV/s in 1 M NH_4Cl.

the aromatic peak compared to that of GABA-NDI [14]. In GABA-NDI at the concentration of 100 mM, the aromatic peak broadened significantly and merged into the baseline of the spectra. The higher hydrophilicity and increased electrostatic repulsion between carboxylate ion groups of ASP in comparison to GABA is suggested as the reason for less self-association [30]. In contrast to the broad first reduction waves reported for neutral NDI derivatives, ASP-NDI shows a sharp, well-defined first redox peak, similar to the -CH_2–COO^- functionalized NDI [17]. Concentration-dependent CVs demonstrate that the peak shape remains essentially invariant from 5 to 50 mM, indicating that ASP-NDI does not undergo the neutral–radical π-stacking that typically broadens the first reduction event [31]. This monomeric behavior is supported by ^{1}H-NMR measurements, where ASP-NDI exhibits only minor aromatic peak broadening even at high concentrations. The two deprotonated carboxylate groups on ASP-NDI at pH ≈7 create strong electrostatic repulsion around the NDI core, preventing the neutral–radical interactions observed in hydrophobic NDIs [32]. In addition, NH_4^+ electrolytes are known to suppress aggregation of anionic organic species, further promoting monomeric redox behavior [15].

2.6 | Computational Studies

To further understand the redox potentials as well as dimerization behavior of ASP-NDI and GABA-NDI, density functional theory (DFT) calculations were initially performed for all monomeric species and their one- and two-electron reduced forms, as well as for dimeric and π-stacked structures. The details of the computational work are given in the section Computational Results in the SI. As the molecules are highly charged, ammonium counterions were included to improve the numerical stability of the calculations and to avoid artificially high charge densities. Although the presence of counterions does not eliminate self-interaction error in DFT, it helps to stabilize highly anionic species and provides a more realistic electrostatic environment. Table 1 summarizes the computed redox potentials for the fully neutralized NDIs.

The results from DFT calculations predict that the addition of two carboxylate groups to the NDI core, when changing from GABA- to ASP-NDI, shifts the reduction potential of the first and second reduction toward positive values. There is reasonable agreement with the experimental values for the first reduction potential, while the second reduction is predicted to be 300–500 mV lower. It is well known that -COOH group acts as an electron withdrawing group while -COO^- group acts as an electron donating group [33, 34]. The pKa of this group is <3, so the carboxyl groups are deprotonated in the studied pH. Electron donating groups increase electron density in the redox active sites of the molecule, making it more difficult to be further reduced. This effect should shift the redox potential toward more negative values, but DFT results show that rule of thumb does not always hold. Optimized geometries for monomeric and dimeric structures shown in Figure 5 show that the carboxylate group of GABA-NDI is bent above the NDI core, while ASP-NDI and B-NDI have geometrically more similar configurations, explaining the differences in DFT redox potentials 17.

Motivated by experimental indications of aggregation, we examined the monomer-dimer equilibria computationally, beginning with the NDI derivatives, considering electroneutrality by explicitly adding NH_4^+ counterions. A hierarchical strategy was employed to separate intrinsic π–π interactions of NDI cores from substituent and charge effects. First, we evaluated the dimerization of the Methyl-NDI core to characterize the "baseline" stacking interaction. The unsubstituted NDI dimer exhibits a solution-phase dimerization Gibbs free energy of −7.11 kcal/mol. Subsequently, we evaluated dimerization for the substituted systems B-NDI, GABA-NDI, and ASP-NDI. In all dimerization calculations, we assumed full neutralization by explicitly adding NH_4^+ counterions. The GABA-NDI monomer is highly compact due to the flexibility of the alkylic substituents, which can adopt geometries that stabilize the counterions via intramolecular hydrogen bonds (Figure S26). This compact arrangement is largely retained in the dimer rather than giving rise to intermolecular hydrogen-bond stabilization. As a result, the dimerization energy remains strong (−7.7 kcal/mol), comparable to the simpler systems. In contrast, ASP-NDI is highly anionic and adopts a more extended, "spread-out" geometry. Even with a single bridging hydrogen bond in the dimer, stabilization is reduced, leading to a weaker dimerization energy of −5.5 kcal/mol. This difference likely reflects the stronger electrostatic repulsion in the highly anionic ASP-NDI system even after neutralization (Figure S27). The lowest-energy dimers identified for the three

TABLE 1 | Computed one- and two-electron reduction potentials (in V vs. SHE) for monomeric NDI derivatives together with counterions.

Compound	1e$^-$ reduction	2e$^-$ reduction	1e$^-$ reduction experimental	2e$^-$ reduction experimental
B-NDI [17] + 2 NH_4^+	−0.45	−0.71	−0.29	−0.47
GABA-NDI [16] + 2 NH_4^+	−0.33	−0.94	−0.12	−0.43
ASP-NDI (this article) + 4 NH_4^+	−0.25	−0.75	−0.30	−0.42

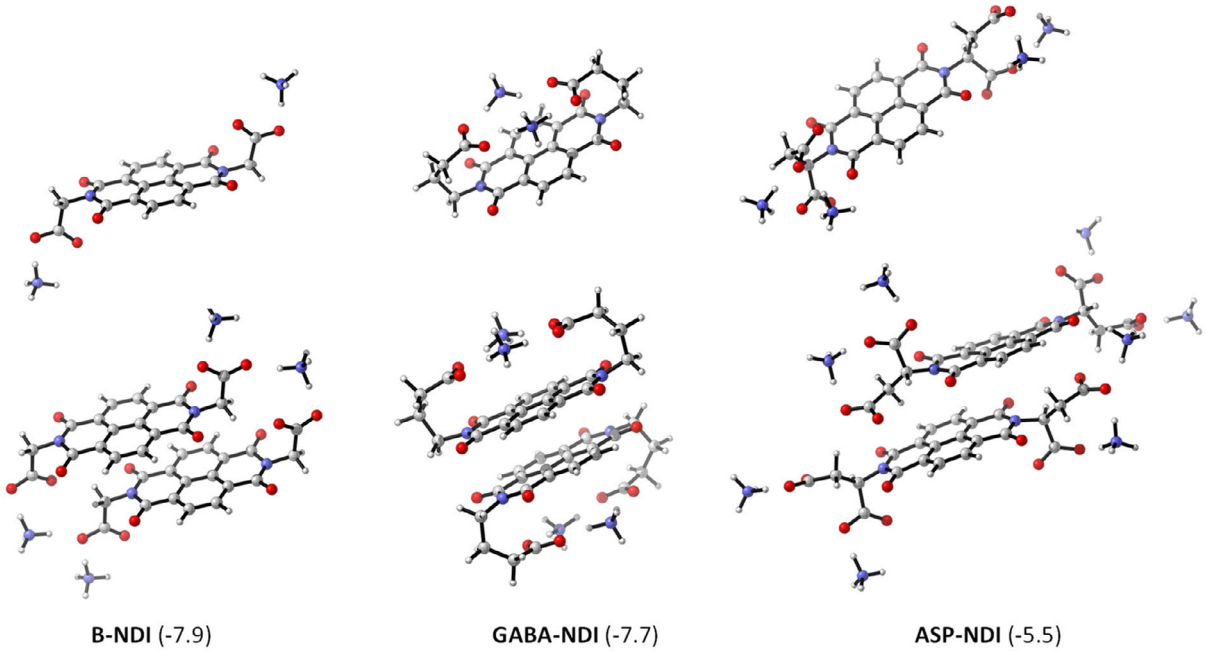

FIGURE 5 | Optimized monomeric and dimeric structures of B-NDI, GABA-NDI, and ASP-NDI. The numbers are the computed aqueous phase Gibbs-free dimerization (as described in Computational methods in SI) energies in kcal/mol.

systems (along with their monomeric structures) are summarized in Figure 5. Because the computed dimerization energies indicate that dimer formation is generally favorable, the reduction potentials of the monomers may be affected by the presence of dimers in solution. To probe these effects, we computed the 1-electron and 2-electron reduced forms of the dimers and evaluated both their dimerization free energies and reduction potentials. Results for GABA-NDI and ASP-NDI are summarized in Table 2.

The columns ΔG^{dimer} provide the intrinsic reaction free energies corresponding to the different possible dimerization pathways. These may not represent the dominant pathway under all solution conditions, particularly if dimers are already present at appreciable concentration. Table 2 also reports the computed reduction potentials for monomers and dimers, enabling comparison between isolated and aggregated species. Although concentration effects cannot be explicitly included in these calculations, the following qualitative interpretation is reasonable: at low concentrations, supposedly the monomers dominate, the observed potentials should be close to monomer values. At higher concentrations, neutral dimers become favored and may influence the electrochemical response before or during reduction. The first reduction stabilizes the GABA-NDI dimer significantly ($\Delta G = -11.25$ kcal/mol). This enhanced stability may arise from improved charge delocalization and increased π-stacking upon reduction. Correspondingly, the $1e^-$ reduction potential of the dimer shifts slightly positive (i.e., reduction becomes easier). This is consistent with a more delocalized electronic structure in the stacked form. For ASP-NDI, the neutral dimerization is −5.5 kcal/mol. Upon one-electron reduction, the dimerization energy becomes −4.16 kcal/mol, indicating that the stabilization is weaker in the reduced dimer compared with the neutral species. While the stacking distance between the NDI cores is similar to that in GABA-NDI, the planes are shifted in ASP-NDI, adopting a more "sandwich-like" geometry. This shift may partly reduce π–π overlap; however, the positioning of the anionic substituents above the aromatic cores could provide some compensating electrostatic stabilization. Consequently, ASP-NDI and GABA-NDI respond differently to aggregation in the one-electron reduction step. Spin-density analyses of the $1e^-$-reduced species confirm that the unpaired electron is fully delocalized across the NDI π-system for all

TABLE 2 | Computed dimerization free energies and redox potentials for GABA-NDI and ASP-NDI monomers and dimers (in V vs. SHE).

			GABA-NDI			ASP-NDI			
Intrinsic dimerization equations	**ΔG^{dimer}, kcal/mol**	—	**Redox potential monomer (V vs. SHE)**	**Redox potential dimer (V vs. SHE)**	**Exp. (V vs. SHE)**	**ΔG^{dimer}, kcal/mol**	**Redox potential monomer (V vs. SHE)**	**Redox potential dimer (V vs. SHE)**	**Exp. (V vs. SHE)**
$M + M \leftrightarrow D$	−7.68			—		−5.52		—	
$M + M^{\cdot -} \leftrightarrow D^{\cdot -}$	−11.25	1st	−0.33	−0.18	−0.12	−4.16	−0.25	−0.31	−0.30
$M^- + M^{\cdot -} \leftrightarrow D^{\cdot 2-}$	−9.23	2nd	−0.94	−0.42	−0.43	0.0	−0.75	−0.43	−0.42
$M + M^{\cdot 2-} \leftrightarrow D^{\cdot 2-}$	−23.26					−11.46			

monomers examined (Figure S29). Upon dimerization, the spin density becomes distributed over both stacked NDI cores, yielding a symmetric, dimer-wide radical delocalization. The second reduction step highlights an even stronger divergence: the intrinsic stability of the doubly reduced ASP-NDI dimer is significantly lower than that of the GABA-NDI dimer. However, if the singly reduced dimers dominate the equilibrium prior to the second reduction, then even ASP-NDI shows a shift toward more positive potentials for the second electron transfer. We note that these NDI derivatives pose nontrivial challenges for electronic-structure methods due to their large, conformationally flexible, and highly charged architectures. In particular, the substantial anionic character and the necessary but intrinsically arbitrary placement of counterions introduce additional uncertainty into the computed thermodynamics. Although the inclusion of counterions improves numerical stability and provides a more realistic electrostatic environment, the resulting energies should still be interpreted as model-dependent. For this reason, the computed values are best viewed as internally consistent trends within the present computational framework, rather than precise quantitative predictions. To summarize, GABA-NDI dimers are consistently more stable than ASP-NDI dimers across all redox states. Dimerization strongly influences the reduction potentials, particularly for the second electron transfer, where allowing dimer formation shifts the potential significantly in the positive direction. ASP-NDI shows weaker dimer stability, with the singly reduced dimer only marginally stabilized and the doubly reduced dimer even partially destabilized. These trends indicate that association effects are substantially more pronounced in GABA-NDI, and they should be taken into account when interpreting its electrochemical behavior. A bar graph illustrating the evolution of reduction potentials under different monomer–dimer equilibria is provided in Figure 6.

2.7 | Flow Battery Measurements

This study examined the performance of four different flow batteries using the same redox couples of ASP-NDI and $Na_4[Fe(CN)_6]$ but at different concentrations and membrane types as listed in Tables S3 and S4 and will be addressed as FB 1–4 in this section. The properties of the membranes used in this work are listed in Table S2. In all of the studied flow batteries, the average cell voltage is 0.816 V (Figure S11), which is 53 mV higher than that of the GABA-NDI based flow batteries. An example of cycling at various current densities (5–60 mA/cm^2) demonstrates fast kinetics, comparable to those observed in previously studied GABA-NDI batteries, as indicated by consistent capacity utilization across this range (Figure S12) [16]. FB 1 (Figure 7 and Figure S13) and FB 3 (Figure 8 and Figure S14) were both assembled with 100 mM ASP-NDI/100 mM $Na_4[Fe(CN)_6]$ electrolytes under similar flow and current conditions and only the membrane was different; FB 1 used Selemion SX-053DK, while FB 3 used Fumasep E-630(K). Despite both being cation-exchange membranes (CEMs), FB 3 showed slightly better performance than FB 1, exhibiting a lower capacity fade of 0.011% per cycle (0.26% per day) compared to 0.017% per cycle (0.38% per day), while maintaining nearly identical energy and coulombic efficiencies (FB 3: EE = 88.64%, CE = 99.97%; FB 1: EE = 87.58%, CE = 99.95%). The two membranes can both transport Na^+, but their anion exclusion seems to be different. Postmortem CV revealed that Selemion SX-053DK permitted some crossover of the negatively charged ferrocyanide species, $[Fe(CN)_6]^{4-}$, into the ASP-NDI side (Figure S17), whereas Fumasep E-630(K) showed no detectable crossover (Figure S18). Interestingly, although Selemion SX-053DK is thicker than Fumasep E-630(K) (Table S2), it displayed both lower resistance (Figure S25) and higher crossover. This combination can be rationalized by its higher water uptake, which reduces resistance but enhances diffusive transport [35]. The fact that FB 3 exhibited only slightly slower capacity fade suggests that membrane selectivity alone does not fully account for the observed decay; additional mechanisms shared by both systems must also contribute, and these will be discussed later in this section. Furthermore, a previous study from our group reported no detectable ferrocyanide crossover through Selemion SX-053DK during extended cycling of a GABA-NDI/ferrocyanide system, but those experiments lasted only 9 and 11 days [16]. By contrast, FB 1 and FB 3 in the present work were operated for 13.6 and 24.7 days, respectively. The appearance of crossover here is therefore consistent with the possibility that anion exclusion in CEMs degrades over time, most likely driven by electroosmotic drag (the transport of water from the negative to the positive side), which can diminish the membrane's effective selectivity [36, 37].

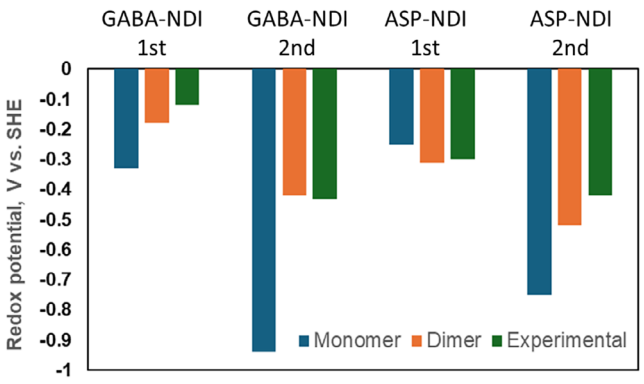

FIGURE 6 | Computed one-electron and two-electron reduction potentials for monomeric (blue) and dimeric (orange) GABA-NDI and ASP-NDI, as well as the corresponding experimental potentials (green). All values are reported in V versus SHE.

At higher electrolyte concentrations (500 mM), the performance gap between the two CEMs was more evident. FB 2, which employed Selemion SX-053DK (Figure 9 and Figure S15), exhibited a capacity fade of 0.036% per cycle (0.175% per day), whereas FB 4, using Fumasep E-630(K) (Figure 10 and Figure S16) showed a far lower fade of 0.010% per cycle (0.0275% per day) despite being operated for a much longer period; nearly 80 days compared to only 10 days for FB 2. Both systems maintained high CE (>99.8%) and similarly high EE (FB 2: 91.11%, FB 4: 87.47%). However, the Selemion membrane again allowed $[Fe(CN)_6]^{4-}$ crossover, which contributed to the degradation of FB 2 over time (Figure S19). In contrast, Fumasep E-630(K) preserved capacity and chemical stability over hundreds of cycles in FB 4 (Figure S20). With a fade rate of only 0.0275% per day, FB 4 represents the most stable NDI-based flow battery reported to date (Table S5). In this study, the higher-concentration systems exhibited lower fade rates than their lower-concentration counterparts. A similar observation was reported by Zhang et al. for other NDI systems [38]. Although that earlier study did not provide an explanation, our postcycling NMR

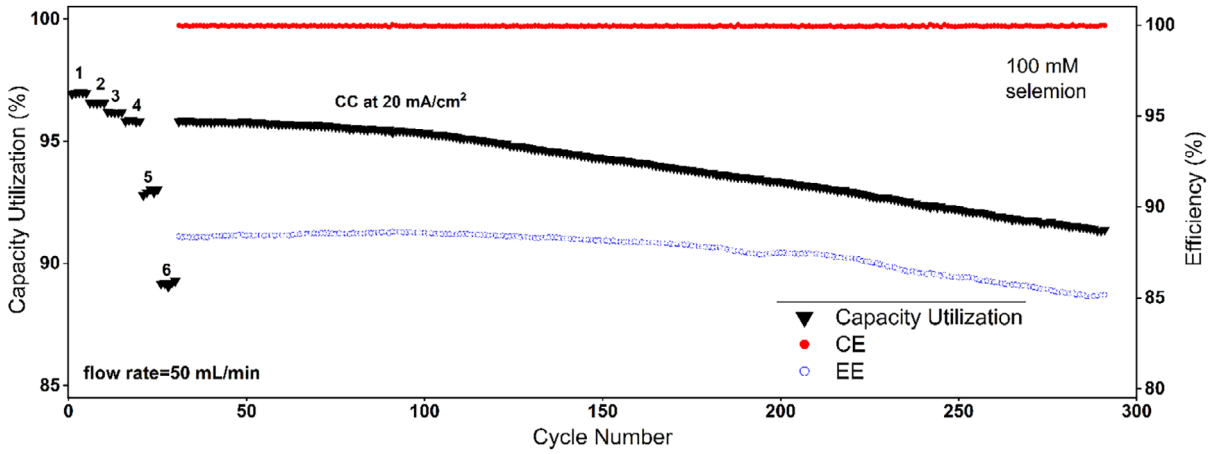

FIGURE 7 | Performance of FB 1- cycling at 1) 5, 2) 10, 3) 15, 4) 20, 5) 40, and 6) 60 mA/cm^2, total cycling time of 13.6 days.

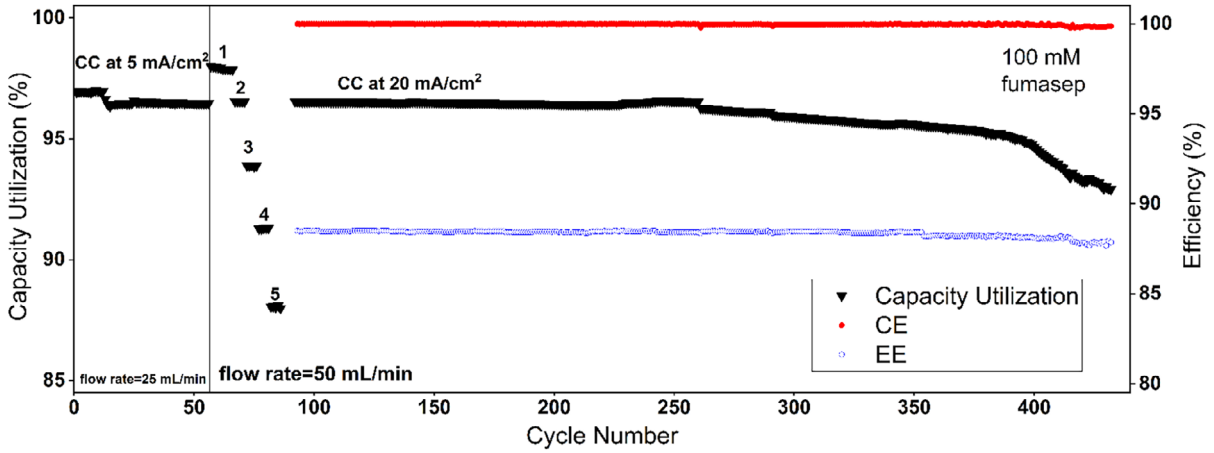

FIGURE 8 | Performance of FB 3- cycling at. 1) 5, 2) 20, 3) 40, 4) 60, and 5) 80 mA/cm^2 total cycling time of 24.7 days.

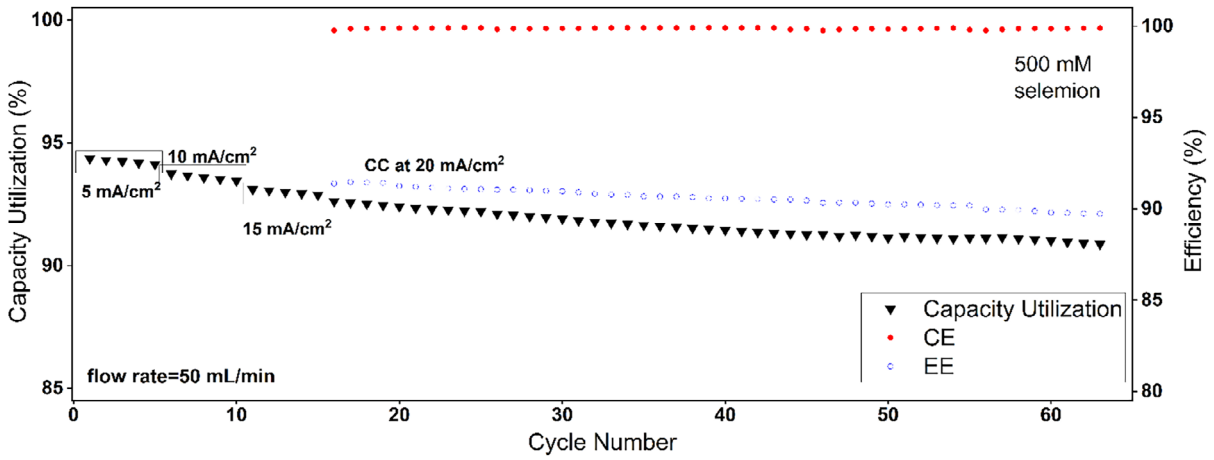

FIGURE 9 | Performance of FB 2 at different current densities, total cycling time of 17.5 days.

results (Figure S21) indicate that capacity loss in this system is not chemically driven. Consequently, the fade rate remains largely independent of active-species concentration, since a chemically induced degradation pathway would be expected to accelerate at higher concentrations. The high capacity utilization in all of the studied NDI based flow batteries, also observed by others, indicates that the self-association of ASP-NDI is not affecting the capacity utilization. This is either because the aggregates are electrochemically active, or the dissociation of the aggregates is sufficiently fast so that monomers are constantly generated to replace those that have reacted in the battery [14]. There are even indications that the self-association itself provides a protective effect for the radical anions that enhances their stability and mitigates undesirable side reactions [28]. As a result, full utilization of the two-electron redox

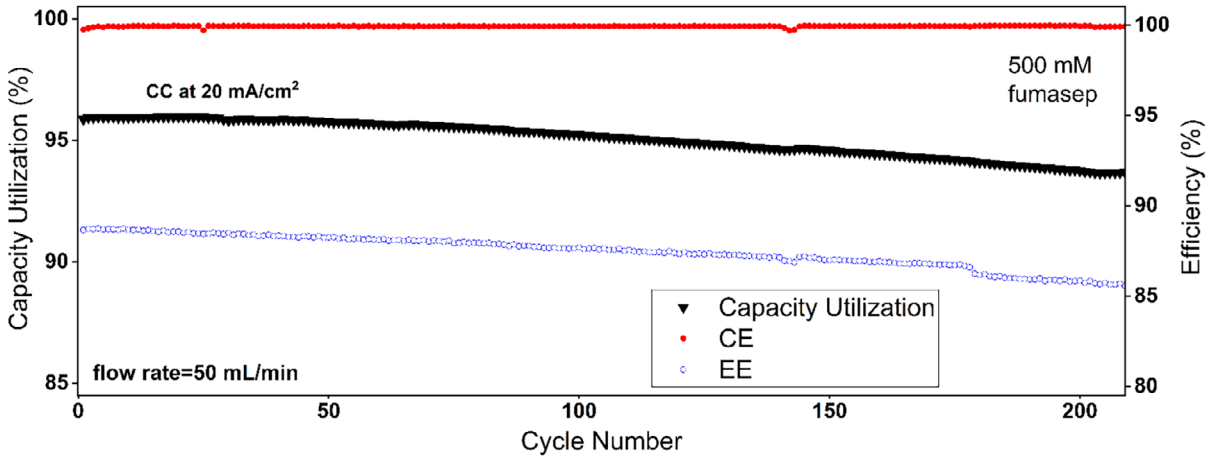

FIGURE 10 | Performance of FB 4 at 20 mA/cm^2, total cycling time of 79.8 days.

capacity of ASP-NDI in a flow battery is possible. This indicates that the optimization of the aggregation behavior is not necessary for achieving high capacity utilization. Finally, to complement the flow battery results, a symmetric flow battery of ASP-NDI was made. The voltage-capacity curves exhibited three distinct plateaus, coming from the presence of two different redox couples (Figure S22). Moreover, the calculated voltage-curve profile matched well with the experimental curves, confirming the validity of the proposed redox mechanism, with more details provided in the Supporting Information (Figure S23). To conclude, in the Selemion-based systems (FB 1 and FB 2), ferrocyanide crossover was the dominant cause of capacity decline. By contrast, the Fumasep-based batteries (FB 3 and FB 4) showed markedly lower fade and substantially longer operational lifetimes, indicating that improved anion exclusion directly translated into enhanced stability. Since NMR analysis revealed no chemical degradation of the NDI species in any of the batteries, it confirms that the losses observed with Selemion arose from crossover rather than molecular decomposition. Overall, while Selemion SX-053DK can initially limit anion crossover, long-term use in aqueous ferrocyanide-containing systems requires careful evaluation, particularly in applications targeting high cycle numbers [39]. Beyond crossover, several physical processes contributed to capacity loss in all systems. Osmotic water transport, electro-osmotic drag, and slow evaporation from the reservoirs by the heat generated from continuous pump operation, gradually altered electrolyte volumes and concentrations. These imbalances reduced accessible capacity even when no active-species crossover occurred and are consistent with the high, stable coulombic efficiencies measured across all of the studied batteries. Long-term operation also revealed a persistent osmotic flux of water from the NDI side to the ferrocyanide side, leading to an increase in the NDI concentration. Over time, this led to local precipitation near electrodes or tubing interfaces, contributing to additional capacity loss and increased flow resistance reflected in declining energy efficiency.

3 | Conclusion

In this work, functionalization of the NDI core with ASP yielded superior performance compared to GABA functionalization, primarily due to the higher water solubility, enhanced chemical stability, and reduced self-association due to the two carboxylate groups. ASP-NDI flow batteries achieved excellent capacity utilization and showed decreased self-association in comparison to GABA functionalized NDI. Membrane selection played a critical role in long-term cycling stability in this work. While Selemion SX-053DK permitted crossover of anionic redox species ($Na_4[Fe(CN)_6]$) leading to gradual capacity fade, Fumasep E-630(K) effectively prevented crossover of both of the active materials, enabling extended cycling stability with minimal capacity loss. At 500 mM of ASP-NDI, the flow battery paired with Fumasep E-630(K) achieved a record-low capacity fade of 0.0275% per day, representing the most stable NDI-based flow battery reported to date. Across all tested flow batteries, coulombic efficiencies remained exceptionally high (≥99.87%), and the observed high energy efficiencies indicated low resistive losses.

4 | Experimental Section

4.1 | Materials

All purchased chemicals in this work were used as received without further purification. KOH, sodium hydroxide, hydrochloric acid, ASP, DMSO, and ether were purchased from Sigma Aldrich. 1,4,5,8-naphthalenetetracarboxylic acid dianhydride was from TCI chemicals.

Acknowledgments

The authors are grateful for the financial support from the Research Council of Finland (BioFlow project, grant agreement 343493), and Jenny and Antti Wihuri Foundation for the homing grant. This work has also partially emanated from the research of P.P. and C.W. supported by the European Research Council (Starting Grant, agreement no. 950038). M.S. and C.W. gratefully acknowledge the PhD Mobility and Researcher Mobility grants from Nordic Energy Research (Nordic Flow Battery Network -project, 100815). A.H. is grateful for the financial support from National Research, Development, and Innovation Office of Hungary (NKFIH grant K-142486). Materials Analysis and Research Infrastructure (MARI) of the University of Turku was utilized in this work.

Open access publishing facilitated by Turun yliopisto, as part of the Wiley - FinELib agreement.

Funding

Research Council of Finland (343493); Jenny ja Antti Wihurin Rahasto H2020 European Research Council (950038); Nordic Energy Research (100815); National Research, Development and Innovation Office of Hungary (K-142486).

Conflicts of Interest

A patent application has been filed with the application number 2451316-0 by Rivus AB.

Data Availability Statement

The data that support the findings of this study are available in the supplementary material of this article.

References

1. M. M. Rahman, M. M. Islam, M. Shafiullah, Md A. Islam, M. A. R. Chowdhury, and Md H. Zahir, "Advancing Grid Integration with Redox Flow Batteries: An Engineering and Economic Review," *Green Chemistry Letters and Reviews* 18 (2025): 2507333.

2. M. Cantera, L. Lubián, K. Cavusoglu, et al., "An Automatized Rebalancing System to Address Faradaic Imbalance and Prolong Cycle Life in Alkaline Ferrocyanide–anthraquinone Redox Flow Batteries," *Batteries & Supercaps* 7 (2024): e202400086.

3. Y. A. Gandomi, D. S. Aaron, J. R. Houser, et al., "Critical Review—experimental Diagnostics and Material Characterization Techniques Used on Redox Flow Batteries," *Journal of the Electrochemical Society* 165 (2018): A970–A1010.

4. A. A. Franco, E. Loup-Escande, G. Loiseaux, et al., "From Battery Manufacturing to Smart Grids: Towards a Metaverse for the Energy Sciences," *Batteries & Supercaps* 6 (2023): e202200369.

5. L. Kortekaas, S. Fricke, A. Korshunov, M. Winter, I. Cekic-Laskovic, and M. Grünebaum, "A Digital Blueprint for 3D-Printing Lab Scale Aqueous and Organic Redox-Flow Batteries," *Batteries & Supercaps* 6 (2023): e202300045.

6. Y. Wang, A. Mu, W. Wang, B. Yang, and J. Wang, "A Review of Capacity Decay Studies of All-Vanadium Redox Flow Batteries: Mechanism and State Estimation," *ChemSusChem* 17 (2024): e202301787.

7. F. Pileri, W. da Silva Freitas, A. D'Epifanio, and B. Mecheri, "Advances in Organic Electroactive Species for Enhancing the Performance of All-Aqueous Redox Flow Batteries in Electrochemical Energy Storage," *Journal of Energy Storage* 113 (2025): 115677.

8. K. Amini, E. F. Kerr, T. Y. George, et al., "An Extremely Stable, Highly Soluble Monosubstituted Anthraquinone for Aqueous Redox Flow Batteries," *Advanced Functional Materials* 33 (2023): 2211338.

9. S. Jin, E. M. Fell, L. Vina-Lopez, et al., "Near Neutral pH Redox Flow Battery with Low Permeability and Long-Lifetime Phosphonated Viologen Active Species," *Advanced Energy Materials* 10 (2020): 2000100.

10. C. de la Cruz, R. Sanz, A. Suárez, E. Ventosa, R. Marcilla, and A. Mavrandonakis, "A Systematic Study on the Redox Potentials of Phenazine-Derivatives in Aqueous Media: A Combined Computational and Experimental Work," *ChemSusChem* 16 (2023): e202201984.

11. A. Korshunov, A. Gibalova, M. Grünebaum, B. J. Ravoo, M. Winter, and I. Cekic-Laskovic, "Host–guest Interactions Enhance the Performance of Viologen Electrolytes for Aqueous Organic Redox Flow Batteries," *Batteries & Supercaps* 4 (2021): 923–928.

12. M. Wu, M. Bahari, Y. Jing, et al., "Highly Stable, Low Redox Potential Quinone for Aqueous Flow Batteries," *Batteries & Supercaps* 5 (2022): e202200009.

13. S. Nandi, L. E. de Sousa, T. Vegge, and P. de Silva, "Degradation of Quinone-Based Flow Battery Electrolytes: Effect of Functional Groups on the Reaction Mechanism," *Batteries & Supercaps* 6 (2023): e202200443.

14. C. Wiberg, F. Owusu, E. Wang, and E. Ahlberg, "Electrochemical Evaluation of a Naphthalene Diimide Derivative for Potential Application in Aqueous Organic Redox Flow Batteries," *Energy Technology* 7 (2019): 1900843.

15. C. Wiberg, L. Evenäs, M. Busch, and E. Ahlberg, "Naphthalene Diimides in Highly Stable pH-Neutral Aqueous Organic Redox Flow Batteries," *Journal of Electroanalytical Chemistry* 896 (2021): 115224.

16. M. Shahsavan, C. Wiberg, and P. Peljo, "Gamma-Aminobutyric Acid-Functionalized Naphthalene Diimide for Aqueous Organic Flow Batteries," *Chemical Communications* 58 (2022): 12692–12695.

17. V. Medabalmi, M. Sundararajan, V. Singh, M.-H. Baik, and H. R. Byon, "Naphthalene Diimide as a Two-Electron Anolyte for Aqueous and Neutral pH Redox Flow Batteries," *Journal of Materials Chemistry A* 8 (2020): 11218–11223.

18. S. Ahn, M. Son, V. Singh, A. Yun, M.-H. Baik, and H. R. Byon, "Stabilization of Naphthalene Diimide Anions by Ion Pair Formation in Nonaqueous Organic Redox Flow Batteries," *Journal of the American Chemical Society* 146 (2024): 4521–4531.

19. X. Liu, H. Zhang, C. Liu, et al., "Commercializable Naphthalene Diimide Anolytes for Neutral Aqueous Organic Redox Flow Batteries," *Angewandte Chemie* 136 (2024): e202405427.

20. M. Pan, W. Wang, H. Wang, J. Ma, M. Shao, and Z. Jin, "High-Voltage and Durable pH-Neutral Aqueous Redox Flow Batteries Based on Quaternary Ammonium Cation-Functionalized Naphthalene Diimide and Nitroxyl Radical Systems," *Journal of Power Sources* 580 (2023): 233269.

21. V. Singh, S. Ahn, and H. R. Byon, "Ammonium-Functionalized Naphthalene Diimides as Two-Electron-Transfer Negolyte for Aqueous Redox Flow Batteries," *Batteries & Supercaps* 5 (2022): e202200281.

22. J. Sun, D. Shi, H. Zhong, X. Li, and H. Zhang, "Investigations on the Self-Discharge Process in Vanadium Flow Battery," *Journal of Power Sources* 294 (2015): 562–568.

23. J. Asenjo-Pascual, I. Salmeron-Sanchez, J. R. Avilés-Moreno, P. Mauleón, P. Mazur, and P. Ocón, "Understanding Aqueous Organic Redox Flow Batteries: A Guided Experimental Tour from Components Characterization to Final Assembly," *Batteries* 8 (2022): 193.

24. B. Hu, J. Luo, M. Hu, B. Yuan, and T. L. Liu, "A pH-Neutral, Metal-Free Aqueous Organic Redox Flow Battery Employing an Ammonium Anthraquinone Anolyte," *Angewandte Chemie International Edition* 58 (2019): 16629–16636.

25. J. Luo, B. Hu, C. Debruler, et al., "Unprecedented Capacity and Stability of Ammonium Ferrocyanide Catholyte in pH-Neutral Aqueous Redox Flow Batteries," *Joule* 3 (2019): 149–163.

26. L. M. Cowen, P. A. Gilhooly-Finn, A. Giovannitti, et al., "Critical Analysis of Self-Doping and Water-Soluble n-Type Organic Semiconductors: Structures and Mechanisms," *Journal of Materials Chemistry C* 10 (2022): 8955–8963.

27. M. B. Kim and D. W. Dixon, "Hydrolysis of Aliphatic Naphthalene Diimides: Effect of Charge Placement in the Side Chains," *Journal of Physical Organic Chemistry* 21 (2008): 731–737.

28. V. Singh, S. Kwon, Y. Choi, et al., "Controlling π–π Interactions of Highly Soluble Naphthalene Diimide Derivatives for Neutral pH Aqueous Redox Flow Batteries," *Advanced Materials* 35 (2023): 2210859.

29. H. Zhang, C. Liu, Z. Wang, et al., "Synergistic Ionic Modification Strategy Enhances the Stability of Naphthalene Diimide Zwitterions for Cost-Effective Aqueous Organic Redox Flow Batteries," *National Science Review* 12 (2025): nwaf123.

30. C. Haese, M. Boecker, A. Vasilev, and M. Mondeshki, "Stability and Self-Association of Styryl Hemicyanine Dyes in Water Studied by ^{1}H NMR Spectroscopy," *Journal of Molecular Liquids* 352 (2022): 118678.

31. B. Kim, J. Lee, Y.-P. Chen, et al., "π-Stacks of Radical-Anionic Naphthalenediimides in a Metal–organic Framework," *Science Advances* 8 (2022): eade1383.

32. A. Pasadakis-Kavounis, V. Baj, and J. Hjelm, "Electrochemical Characterization of Aromatic Molecules with 1,4-Diaza Groups for Flow Battery Applications," *Molecules* 26 (2021): 2227.

33. D. P. Tabor, R. Gómez-Bombarelli, L. Tong, R. G. Gordon, M. J. Aziz, and A. Aspuru-Guzik, "Mapping the Frontiers of Quinone Stability in Aqueous Media: Implications for Organic Aqueous Redox Flow Batteries," *Journal of Materials Chemistry A* 7 (2019): 12833–12841

34. W. Wu, A. P. Wang, J. Luo, and T. L. Liu, "A Highly Stable, Capacity-Dense Carboxylate Viologen Anolyte toward Long-Duration Energy Storage," *Angewandte Chemie International Edition* 62 (2023): e202216662.

35. C. J. Van Cauter, Y. Li, S. Van Herck, I. F. J. Vankelecom, "Stability and Performance of Commercial Membranes in High-Temperature Organic Flow Batteries," *Membranes* 14 (2024): 177.

36. L. J. Small, H. D. Pratt, and T. M. Anderson, "Crossover in Membranes for Aqueous Soluble Organic Redox Flow Batteries," *Journal of the Electrochemical Society* 166 (2019): A2536–A2542.

37. K. Oh, M. Moazzam, G. Gwak, and H. Ju, "Water Crossover Phenomena in All-Vanadium Redox Flow Batteries," *Electrochimica Acta* 297 (2019): 101–111.

38. X. Zhang, X. Liu, Z. Wang, et al., "Multi-Hydrogen-Bond-Engineered Imidazolium-Functionalized Naphthalene Diimides for Stable Two-Electron Storage in Aqueous Organic Flow Batteries," *Energy Storage Materials* 81 (2025): 104527.

39. M. T. Tsehaye, G. Mourouga, T. J. Schmidt, et al., "Towards Optimized Membranes for Aqueous Organic Redox Flow Batteries: Correlation between Membrane Properties and Cell Performance," *Renewable and Sustainable Energy Reviews* 173 (2023): 113059.

Supporting Information

The authors have cited additional references within the Supporting Information. Additional supporting information can be found online in the Supporting information section. **Supporting Fig. S1:** 1H-NMR spectra of ASP-NDI (80 MHz, H2O) 8.602 (s, 4H), 5.899-5.718 (q, 2H), 3.291-2.593 (m, 4H). **Supporting Fig. S2:** LC/MS on the synthesized molecule – fragmentation. **Supporting Fig. S3**: LC/MS on the synthesized molecule – evidence of mono-substituted molecule. **Supporting Fig. S4:** 1H-NMR spectra of the solubility test using 2,3,5,6-tetramethylpyrazine as an internal reference. **Supporting Fig. S5:** Concentration-normalized CV of ASP-NDI in 1 M NH4Cl at 50 mV/s. **Supporting Fig. S6:** Reduction potentials and the peak separation calculated from Figure S5. **Supporting Fig. S7:** Levich analysis. **Supporting Fig. S8:** Pourbaix diagram of ASP-NDI (data extracted from Figure 3). **Supporting Fig. S9:** 1H-NMR spectra of 5 mM of pristine ASP-NDI and ASP-NDI in pH 10.5 after 24 hours. **Supporting Fig. S10:** 1H-NMR spectra of different concentrations of ASP-NDI and GABA-NDI in 1 M NH4Cl. **Supporting Fig. S11:** CVs of 5 mM ASP-NDI and 5 mM Na4[Fe(CN)6] in 1 M NH4Cl at 50 mV/s and the average voltage between them. **Supporting Fig. S12:** Representative charge/discharge curves of ASP-NDI/ Na4[Fe(CN)6] flow battery (negative electrolyte: 10.5 mL of 100 mL ASP-NDI, positive electrolyte: 33 mL of 100 mM Na4[Fe(CN)6], supporting electrolyte: 1 M NH4Cl and 0.5 M ammonium phosphate buffer at pH 7.9). **Supporting Fig. S13:** Performance of FB 1. **Supporting Fig. S14:** Performance of FB 3. **Supporting Fig. S15:** Performance of FB 2. **Supporting Fig. S16:** Performance of FB 4. **Supporting Fig. S17:** CV of ASP-NDI and Na4[Fe(CN)6] after FB 1 at 100 mV/s in 1 M NH4Cl and 0.5 M ammonium phosphate buffer. **Supporting Fig. S18:** CV of ASP-NDI and Na4[Fe(CN)6] after FB 3 at 100 mV/s in 1 M NH4Cl and 0.5 M ammonium phosphate buffer. **Supporting Fig. S19:** CV of ASP-NDI and Na4[Fe(CN)6] after FB 2 at 100 mV/s in 1 M NH4Cl and 0.5 M ammonium phosphate buffer. **Supporting Fig: S20:** CV of ASP-NDI and Na4[Fe(CN)6] after FB 4 at 100 mV/s in 1 M NH4Cl and 0.5 M ammonium phosphate buffer. **Supporting Fig. S21:** Post-test 1H-NMR after long-term FB battery testing of ASP-NDI negolytes, including a pristine reference negolyte (1: FB 1, 2: FB 2, 3: FB 3, 4: FB 4, 5:ASP-NDI before cycling). **Supporting Fig. S22:** Representative charge/discharge curves of symmetric ASP-NDI flow battery (negative electrolyte: 12 mL of 500 mL ASP-NDI, positive electrolyte: 20 mL of 500 mM ASP-NDI, supporting electrolyte: 1 M NH4Cl and 0.5 M ammonium phosphate buffer at pH 7.9). **Supporting Fig. S23:** Experimental (black) and calculated (pink) voltage-capacity profiles of the symmetric ASP-NDI flow battery during cycle 3. **Supporting Fig. S24:** Performance of symmetric ASP-NDI flow battery (negative electrolyte: 12 mL of 500 mL ASP-NDI, positive electrolyte: 20 mL of 500 mM ASP-NDI, supporting electrolyte: 1 M NH4Cl and 0.5 M ammonium phosphate buffer at pH 7.9, cycling for 17.5 days at 20 mA/cm2). **Supporting Fig. S25:** Nyquist plots for EIS of the studied flow batteries in this work before and after cycling. **Supporting Fig. S26:** Different GABA-NDI dimer arrangements. The numbers in the parenthesis are aqueous Gibbs free energies relative to the most stable dimer conformation (in kcal/mol). **Supporting Fig. S27:** The most stable ASP-NDI dimer, and the compact analogue to the GABA-NDI dimer without bridging H-bonds. The numbers in the parenthesis are aqueous Gibbs free energies relative to the most stable dimer conformation (in kcal/mol). **Supporting Fig. S28:** Optimized monomeric and dimeric structures of Me-NDI, B-NDI, GABA-NDI and ASP-NDI. The numbers in parenthesis are the computed aqueous phase Gibbs-free dimerization energies ($\Delta G^{\mathrm{dimer}}$) in kcal/mol. **Supporting Fig. S29:** Spin-density plots of the optimized one-electron reduced monomeric (top) and dimeric (bottom) GABA-NDI and ASP-NDI species (the isovalue = 0.0004 a.u. was used for the density map). **Supporting Fig. S30:** Spin-density isosurface (isovalue = 0.0004 a.u.) of the open-shell singlet broken-symmetry solution of the two-electron reduced ASP-NDI dimer. The α-β spin-density difference is shown, illustrating the symmetric localization of opposite spins on the two π-stacked NDI cores. **Supporting Table S1:** Calculated Diffusion coefficients at different concentrations based on the data from Figure S5. **Supporting Table S2:** Membranes used in this work and their characteristics. **Supporting Table S3:** Details of battery experiments for FB1 & FB2 with Selemion membrane. **Supporting Table S4:** Details of battery experiments for FB3 & FB4 with Fumasep membrane. **Supporting Table S5:** NDI derivatives studied in flow batteries. **Supporting Table S6:** Computed one- and two-electron reduction potentials (in V vs. SHE) for monomeric NDI derivatives in different charge states. C2, C1, and C0 correspond to the fully neutralized, partially neutralized, and no-counterion forms, respectively. For ASP-NDI, C4 and C3 denote four and three NH_4^+ counterions. Potentials were computed using solution-phase Gibbs free energies from the DFT protocol described above. **Supporting Table S7:** Computed relative energy data of different spin states for optimized two-electron reduced ASP-NDI confomers. Notation: $E_{\mathrm{def2\text{-}TZPP}}$ is the single-point electronic energy computed with the larger basis set def2-TZVPP, and G is the solvent-phase Gibbs free energy. All values are reported relative to the most stable conformation in terms or Gibbs free energy (in kcal/mol). **Supporting Table S8:** Computed energy data of the optimized structures at B3LYP/def2-SVP (SMD, water), employing the Becke-Johnson dispersion damping function, where the notations are: $E_{\mathrm{def2\text{-}SVP}}$ is the electronic energy computed by using the basis set def2-SVP, $E_{\mathrm{def2\text{-}TZPP}}$ is the single point energy computed with the larger basis se def2-TZVPP and $G(RRHO)_{\mathrm{def2\text{-}SVP}}$ and $G(QRRHO)_{\mathrm{def2\text{-}SVP}}$ are the thermal contributions computed in the RRHO and quasi-RRHO approximation. G is calculated as: $G = E_{\mathrm{def2\text{-}TZVPP}} + (G(QRRHO)_{\mathrm{def2\text{-}SVP}} - E_{\mathrm{def2\text{-}SVP}}) + 0.0030119$ (in a.u.). All Cartesian coordinates of the optimized structures used in this work are provided in the supplementary file computed_structures.zip. The file uses the same structural labels as presented in Table S8.